Investigations in nanosecond laser micromachining on the $Zr_{52.8}Cu_{17.6}Ni_{14.8}Al_{9.9}Ti_{4.9}$ bulk metallic glass: experimental and theoretical study

Yang Jiao, Emmanuel Brousseau*, Quanquan Han, Hanxing Zhu, Samuel Bigot

Cardiff School of Engineering, Cardiff University, Cardiff, United Kingdom, CF24 3AA

Abstract: In addition to their attractive mechanical properties, the lack of grain boundaries and crystal defects of Bulk Metallic Glasses (BMGs) make them suitable materials for integration in micro-systems fabrication chains, either as final components or mould inserts. The application of short or ultra-short pulsed lasers has recently been demonstrated for the processing of BMGs in this context, particularly as a possible solution for machining micro-scale features on the surface of BMG workpieces. Therefore, complementary studies that consider both experimental and thermal simulation data at the same time in the context of multiple and moving pulses irradiating a BMG specimen are desirable to gain insight into micromachining phenomena. Although such models have been reported in the context of single pulse processing of BMG substrates, their extension to multiple pulse scenarios for micromachining is lacking. Thus, the overall objective of this paper is to combine both theoretical and experimental laser micromachining investigations using multiple pulses when irradiating a BMG workpiece. The specific focus is on conducting such laser operations in the nanosecond regime on a Zr-based BMG, with composition $Zr_{52.5}Cu_{17.9}Ni_{14.6}Al_{10}Ti_5$, also known as Vitreloy 105. This combined experimental and theoretical approach enabled the identification of a suitable set of laser parameters with respect to the process efficiency over a range of pulse duration, fluence values, scanning speed and track distance between machined grooves. In addition, it was highlighted that laser micro-machining operations can lead to BMG materials experiencing thermal cycles, which are quite different from that taking place during the conventional synthesis of glassy alloys, thus complicating the further characterisation and understanding of crystallisation phenomena at play.

Keywords: bulk metallic glass; nanosecond laser micromachining; multiple and moving pulses; experimental and theoretical study

1. Introduction

Bulk Metallic Glasses (BMGs), which are amorphous alloys made of metallic elements, combine some characteristics of both glasses and metals. These alloys display a unique atomic structure that features a lack of long-range order and which results in the absence of crystal defects and grain boundaries. These specific characteristics lead to BMGs exhibiting excellent mechanical properties, such as high yield strength (Loffler, 2003), high hardness (Wang et al., 2004), good wear resistance (Ashby and Greer, 2008), large elastic limit (Cheng and Ma, 2011) and excellent corrosion resistance (Zhang et al., 2018) as well as improved magnetic properties (Chen, 2011). Consequently, BMGs have been considered potential candidate materials for several applications, such as golf heads (Inoue et al., 2011) and pressure sensors (Inoue et al., 2014). BMGs are also particularly attractive for the manufacturing of micro-components, such as micro-gears (William and Johnson, 1999) and micro-electromechanical systems (MEMS) (Schroers et al., 2007) because their lack of crystal structure favours homogenous processing conditions. A number of material removal technologies for micro and nano-scale fabrication have been applied on BMG substrates, such as mechanical machining (Kuriakose et al., 2017) and focussed ion beam (FIB) milling (Zhang et al., 2016). However, mechanical machining can lead to high tool wear and crystallisation of the machined area (Samant and Dahotre, 2009) while FIB milling has a low efficiency in addition to the common associated issue of ion implantation.

Processing with high-power lasers, on the other hand, provides an alternative solution that can overcome such limitations. Thus, it is perhaps not surprising that several applications of laser irradiation of BMG materials have been reported in the past 20 years, as described in a recent review on the subject (Williams and Lavery, 2017). These applications include laser welding, laser additive manufacturing, laser surface treatment and laser micromachining. For example, Kim et al. (2006) were the first to successfully demonstrate the laser welding of two Cu-based metallic glass parts. The adoption of lasers in this case is beneficial to overcome the size restriction of cast BMG parts. More recently, BMGs have

also been studied in the context of laser-based additive manufacturing. The work of Yang et al. (2012), for instance, reported the application of laser melting where layers of a Zr-based amorphous powder were successively deposited and then irradiated to eventually form a solid 3-dimensional component. Laser technology also has been investigated to improve the surface properties of metallic glass parts, via both laser surface melting (LSM) and laser shock peening. Chen et al. (2010) succeeded in enhancing the plasticity of a Zr-based BMG specimen by applying LSM and attributed this improvement to the re-distribution of residual stress. Lasers can also be employed to modify the surface performance of a substrate but this time in a "cold" manner via laser shock peening, as is already widely realised for the surface modification of aero-engine materials (Nie et al., 2014). Fu et al. (2014) treated a Zr-based BMG substrate in this way and found that the induced residual stress contributed to the improvement in plasticity of the BMG material.

The application of lasers for the micromachining of BMGs, which is the specific focus of the research reported here, has also been investigated by a few researchers. The literature on this subject can broadly be categorised into single and multiple pulse studies. For single pulse irradiation, the majority of the work has been targeted at the understanding of the surface morphology in and around individual craters. In this context, Liu et al. (2011) and Zhu et al. (2016) mainly concentrated their efforts on the peculiar formation of surface ripple patterns outside isolated craters when irradiating a well-known Zr-based BMG substrate, namely Vitreloy 1, with a single ns pulse. Liu et al. (2011) also conducted a study in the ns regime with a similar purpose but on another type of Zr-based BMG. The surface morphological evolution within craters generated on a slightly different Zr-based BMG composition was also studied by Ma et al. (2010). A key difference compared to related single pulse studies is that these authors used a fs laser to deliver successive pulses on the same spot. This led to the formation of three types of concentric rings structures within the irradiated area depending on the laser fluence and the number of pulses delivered. The surface morphology of single craters was also the focus of the work from Williams and Brousseau (2016) in the context of single ns laser irradiation of Vitreloy 1. In contrast to the investigations reported earlier, these authors also analysed the output of a thermal model, which could predict temperature profiles under different laser parameter conditions, as a means to support the interpretation of experimental observations. It is worth noting that Jiang et al. (2015) and Quintana et al. (2009) also reported single pulse experiments on amorphous metals but not for the specific purpose of studying crater morphology. More specifically, the work from Jiang et al. (2015) was targeted at the understanding of the explosive boiling process when irradiating a Vitreloy 1 specimen with a ns pulse while Quintana et al. (2009) explored whether the single pulse ablation of a Ni-based amorphous material could lead to the formation of crystalline precipitates. To achieve this, a foil 40 µm thick was used as the workpiece and experiments were conducted both in the ps and µs regimes. The results showed that single pulse irradiation in both regimes did not lead to crystallisation of the amorphous sample.

Exploring the microstructure of BMG specimens after laser processing was also the aim of a few reports in the second category of studies of interest here, i.e. those concerned with multiple and moving pulses for achieving laser milling, drilling or cutting operations. Lin et al. (2012) successfully used a ns laser to cut a Mg-based BMG while being able to maintain its amorphous nature by appropriately controlling laser power and scan speed. Wang et al. (2007) performed several laser micromachining operations, namely drilling and trenching, of a Zr-based amorphous alloys using fs laser pulses. In this regime, these authors found that crystallization, molten trace and spatter could be avoided. In the area of multiple pulse micromachining of BMGs, it is also of interest to mention two studies that reported the application of laser processing as one possible step in a process chain to fabricate micro-components. These include the work of Chen et al. (2013), who demonstrated the machining of periodic micro and nano-structures on a Pd- and Ni-based BMG using a fs laser and also, the work of Vella et al. (2015). These latter authors described the successful application of ps and ns laser processing to produce patterns in a Vitreloy 1b BMG workpiece, which was subsequently used as a mould for the replication of micro-structured polymer components.

The study presented in this paper aims to contribute to these research efforts in laser micromachining of BMGs using multiple moving pulses given the potential application of this technique for the manufacturing of micro-components. Based on the literature reported above, it can be said that investigations in the laser processing of BMGs with multiple pulses have essentially been experimental in nature. Thus, the objective of this research is to conduct a combined theoretical and experimental

study in this specific context. This is achieved by further developing the thermal model reported in the single pulse work of Williams and Brousseau (2016) to simulate the incident energy from multiple and moving pulses. It is anticipated that knowledge of the theoretical thermal history of a BMG substrate can assist in the selection of appropriate laser processing parameters. Also, it is expected that by combining experimental observations and theoretical outcomes, an enhanced understanding of the laser micromachining of BMG specimens could be achieved. In this study, a ns fibre laser was used to machine a commercial Zr-based BMG, namely Vitreloy 105, with different laser parameters. A numerical simulation model that incorporates temperature dependent thermo-physical properties and transient physical process is also developed to predict the thermal behaviour. The underlying material removal mechanism and the influence of laser parameters are discussed according to the temperature evolution during the process. Finally, the material removal rate (MRR) achieved during laser milling operations is analysed based on the distance between two linear tracks, once all other parameters have been determined.

2. Numerical modelling and experimental procedures

2.1 Computational modelling

Given the very short laser material interaction time in the ns regime, it is difficult to conduct in-situ experimental measurements to capture accurately thermal effects during processing. For this reason, a finite element (FE) based numerical computational model was developed with the commercial software platform, COMSOL™. A two-dimensional theoretical model was created to analyse the temporal and spatial evolution of the temperature on the surface, and within, the target material. This model was also used to predict the thermal history of the BMG specimens and the dimensions of machined craters when processed under different laser parameters.

In the ns regime, when the laser beam is irradiated on a surface, the delivered energy is absorbed by electrons within the lattice during a time length, which is shorter than the pulse duration. This means that the energy absorbed by the target material can be regarded as being transformed instantaneously into heat (Ready, 1965 and Vora et al., 2013). Therefore, the constitutive equation used in this study was the classic Fourier heat equation (Steen and Mazumder, 2010). In addition, it was assumed that the laser energy followed a Gaussian distribution both temporarily and spatially. Furthermore, the laser intensity decay along the depth of the irradiated material can be described by the Beer-Lambert Law (Hitz et al. 2012).

Consequently, the heat input, $P(x,t)$, in the developed model was expressed as follows:

$$P(x,t) = \alpha \times (1-R) \times P_0 \times e^{-2\left(\frac{x-x_0}{r}\right)^2} \times e^{-4\times ln2\times\frac{(t-t_0)^2}{(t_p)^2}} \times e^{-\alpha z} \quad (1)$$

where α represents the absorption coefficient $(1/m)$, R denotes the reflectivity, P_0 is the peak output intensity of the pulsed laser (W/m^2), x is the coordinate along the surface of the irradiated material (m), x_0 denotes the centre of the laser spot (m), r is the radius of the laser beam at the focal point (m), t_0 represents the time at which the pulse starts (s), t_p is the full duration of the pulse at half maximum (s), and z is the coordinate along the depth (m).

The peak output intensity, P_0, is described as:

$$P_0 = \frac{E}{(\pi r^2 \times t_p)} \quad (2)$$

where E is the pulsed laser energy (J).

In this model, the heat loss resulting from the latent heat of fusion and the induced ablation are considered by introducing a heat flux term, q_a, as a thermal boundary condition. This term is expressed as:

$$q_a = h_a(T_m - T) \quad (3)$$

where T is the material temperature, T_m is the melt temperature and h_a is a temperature dependent heat transfer coefficient, which is expressed with a ramp function equal to zero when $T < T_m$ and that increases linearly as $T > T_m$.

The prediction of the topography of single craters was achieved using a COMSOL™ built-in module named "deformed geometry". In particular, the volume in the material for which the temperature is computed to be above T_m is removed from the target material and the remaining profile is taken as the crater topography. In order to improve the modelling accuracy, the specific heat capacity, C_p $(J/(kg\ K))$, and the thermal conductivity, k $(W/(m\ K))$, of Vitreloy 105 were set to be temperature dependent. However, the density, ρ, and the absorption coefficient, α, were kept constant. Natural convection cooling and radiation were also incorporated in the model as boundary conditions. The specific values of the physical parameters used in this model are given in Table 1. Finally, to simulate multiple and moving pulses conditions, the workpiece was defined to be stationary while the heat input was also modelled in COMSOL™ to be applied at regular time and space intervals along the x coordinate. More specifically, for the space interval, the position of the centre point of different laser spots along the x-axis is simply obtained by the product between the scanning speed and the period, while its z coordinate is kept constant. Regarding the time interval between pulses, an analytical function, β, is used, which is defined as:

$$\beta = Gauss\_time(mod(t, 1/f)) \tag{4}$$

where $Gauss\_time()$ is a temporal Gaussian function of the laser-induced heat input, $mod()$ is a built-in periodic function available in the COMSOL™ software and f is the frequency of the pulsed laser. The function $Gauss\_time()$ is simply expressed as:

$$Gauss\_time = e^{-4\times ln2\times\frac{(t-t_0)^2}{(t_p)^2}} \tag{5}$$

for which the parameters have been defined earlier in this section before.

Table.1. Material property values used for the $Zr_{52.8}Cu_{17.6}Ni_{14.8}Al_{9.9}Ti_{4.9}$ BMG

Material Property Parameter (units)	Symbol	Parameter Value	Source
Density (g/cm^3)	P	6.73	Bian et al. (2002)
Glass Transition Temperature (K)	T_g	675	Glade et al. (2000)
Crystallization Temperature (K)	T_x	727	Glade et al. (2000)
Melting Point (K)	T_m	1069	Glade et al. (2000)
Specific Heat Capacity (J/(kg K))	C_p	$(1/M) \times (24.9 + 11.2\times 10^{-3}T + 6.43 \times 10^6/T^2)$	Glade et al. (2000)
Thermal Conductivity (W/m K)	K	$0.0163T + 0.84$	Demetriou and Johnson (2004)
Heat transfer coefficient (W/m^2 K)	h_a	100	Kannatey-Asibu (2009)
Emissivity	ε	0.35	Kolev (2012)
Molar mass (kg/mol)	M	0.0729	

Note: The value of the thermal conductivity, k, adopted in this study was that of Vitreloy 1 due to the absence of any published data for this thermal property for Vitreloy 105.

2.2 Material

The BMG material investigated in this work is commonly referred to as Vitreloy 105 and has a nominal composition $Zr_{52.8}Cu_{17.6}Ni_{14.8}Al_{9.9}Ti_{4.9}$ (at%). The Vitreloy 105 specimens were commercially available and produced by the company Visser Precision (Denver, USA). These were cast using vacuum injection moulding to produce rods, which were 3 mm in diameter and 10 mm in length. Thus, the BMG parts processed in this study exhibited the interesting characteristic of being synthesised with an industrial process rather than a laboratory-based technique. In addition, the selection of the Vitreloy 105 material was also motivated by the fact that 1) it contains neither toxic elements nor precious metals, in comparison with its better-known cousin, Vitreloy 1, and 2) it exhibits excellent fatigue characteristics among most BMG compositions, as reported by both Peter et al. (2002) and Naleway et al. (2013). The specimens used for the laser experiments were cut from the as-cast 10 mm long cylindrical rods with

micro wire electrical discharge machining to obtain samples 3 mm in diameter and 4 mm thick, as shown in Fig. 1. The structure of the as-fabricated alloys was characterised by X-ray diffraction (XRD) with Cu K_α (λ=1.789 Å) radiation at 35 kV and 40 mA in continuous scan mode. As can be seen in Fig. 1, the XRD pattern of the as-cast specimens shows an overall amorphous halo and two crystalline peaks within the glassy matrix. Thus, it can be said that the specimens were not fully amorphous as they contained a crystalline phase, which was identified as $CuZr_2$. Prior to the microstructural characterisation with XRD and the laser processing experiments, the planar surfaces of the specimens were polished using 1200 and 2000 grid SiC papers followed by a final step using a 1 µm diamond gel suspension until a mirror-like appearance was achieved. The specimens were also cleaned with acetone in an ultrasonic bath for 15 minutes to remove impurities and small particles from their surface.

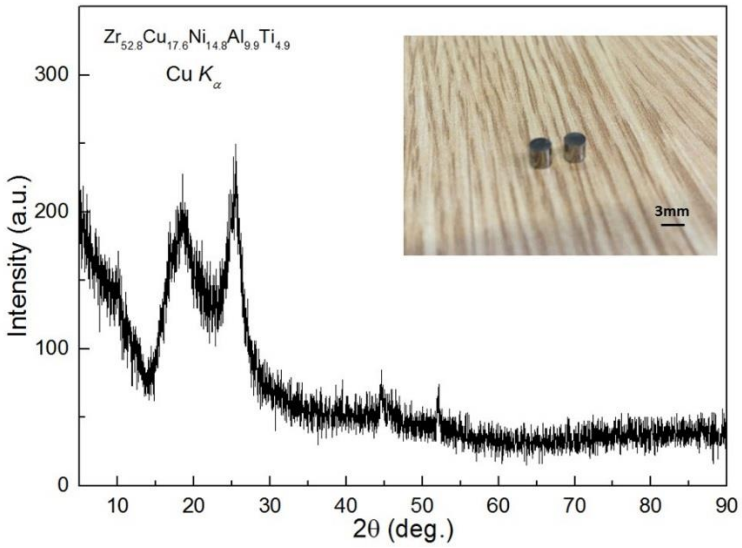

Fig. 1. XRD pattern and photo (inset) of Vitreloy 105 metallic glass specimens

2.3 Laser processing

The system utilised in this study was a fibre laser with 20 W output power manufactured by SPI Lasers (Southampton, United Kingdom). The actual spatial profile of the intensity of the delivered laser beam was near Gaussian with an M^2 value less than 2 while the focal length was 100 mm. In order to calculate the delivered fluence, the effective diameter of the laser spot was estimated first. Using the method presented by Liu (1982), it was found to be 32 µm. This was described in more details in our previous work by Williams and Brousseau (2016). The delivered laser fluence was then calculated by dividing the laser energy per pulse by the laser spot area.

Several waveforms corresponding to different pulse durations were employed, namely 65 ns, 140 ns and 220 ns. A range of different laser fluence values, scanning speeds and track distances were also considered for each pulse length. The laser machining operations were conducted in ambient atmosphere. Machined cavities can be achieved by translating the motion platform of the system in x, y and z directions. As illustrated in Fig. 2, the laser beam travelled from a given starting edge of the area defining a cavity and moved to a finishing edge in the x direction for a distance *L*, thus completing one track. The first irradiated spot for the subsequent track was set at a distance increment, D_s, of several micrometres in the y direction. This process was repeated until a whole rectangular area was machined. Even though the depth machined in this manner for one layer is only a few micrometres, a cavity could be achieved in a layer-by-layer sequence using multiple linear laser tracks.

One issue in laser machining is the varying surface height of the specimen as material removal progresses, which affects the positioning of the surface at the focal length. To overcome this with the laser system utilised, a built-in probe was used to detect the specimen surface automatically after removing one layer. The three waveforms considered in this research along with their pulse duration and their maximum pulse energy, E_{max} , achievable at the optimal pulse repetition rate (PRF0) are

shown in Table 2. For each waveform, operating the laser at frequency values equal to or below the PRF0, ensured that the pulse energy selected remained constant regardless of the range of frequencies considered. In order to guarantee the reliability of the data, all experiments were repeated three times. The detailed laser parameters used in present study are shown in Table.3.

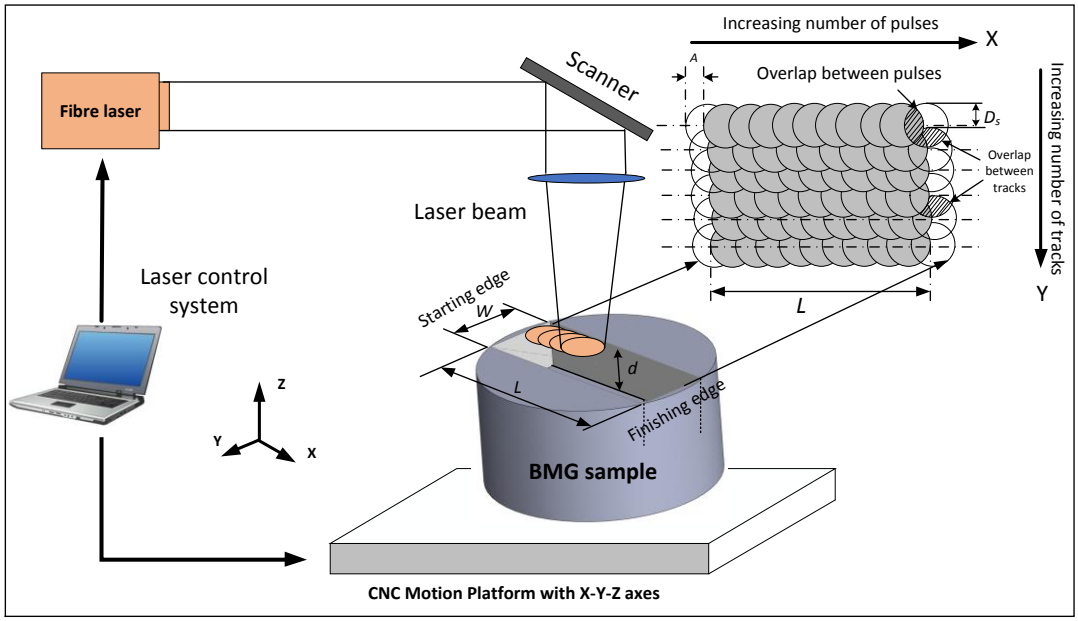

Fig. 2. Schematic diagram of the laser machining process

Table.2. Preset waveforms with their corresponding pulse duration, PRF0, and the maximum energy at PRF0

Waveform number	Pulse duration (ns)	PRF0 (kHz)	E_{max} (mJ) at PRF0
11	220	35	0.57
16	140	51	0.39
22	65	80	0.25

Table.3. Detailed laser parameter used for the laser irradiation experiments

Wavelength (nm)	Spot diameter (μm)	Laser fluence (J/cm²)	Pulse duration (ns)	Frequency (kHz)	Scanning speed (mm/s)	Track distance (μm)	Machining operations
1064	32	30	220	35	-	-	Single pulse
		30	140	51	-	-	
		30	65	80	-	-	
		10	220	35	-	-	
		20	220	51	-	-	
		40	220	80	-	-	
		50	220	35	-	-	
		60	220	35	-	-	
		70	220	35	-	-	
		30	220	35	100	-	Multiple pulses; machining of grooves
		30	220	35	200	-	
		30	220	35	300	-	
		30	220	35	200	5	Multiple pulses; machining of cavities
		30	220	35	200	7	
		30	220	35	200	10	
		30	220	35	200	12	
		30	220	35	200	15	

2.4 Experimental characterisation techniques

A scanning electron microscope (1540XB from Carl Zeiss, Germany) was used to examine the surface topography of the processed specimens from a qualitative perspective. An Atomic Force Microscope (XE-100 from Park Systems, South Korea), a 3D optical microscope (Sensofar, Spain) and a Talysurf instrument (AMETEK, United States) were used to measure the size of the laser machined singe craters, grooves and cavities, respectively. In order to determine the size of the crater, the boundary of the crater was defined at the point where the height of the crater edge, prior to the crater rim, was the same as that of the height of the surface of the sample as illustrated with a typical example in Fig. 3. Besides, three measurements of depth and diameter were taken for each crater and the average values were then used. The efficiency of machining a cavity was assessed by calculating the material removal rate for one layer, MRR, as follows (Wang and Zeng, 2007):

$$MRR = \frac{\rho \times L \times W \times d}{t_{processing}} \tag{6}$$

where ρ is the density of Vitreloy 105, L is the length of the cavity, W is the width of the cavity and d is the depth of a removed layer, which was measured with the Talysurf instrument, and $t_{processing}$ is the total processing time defined as the time when the laser beam is on.

For machining one layer, $t_{processing}$ is given by:

$$t_{processing} = N_{pulses} \times N_{tracks} \times t_p \tag{7}$$

where t_p is the pulse duration, N_{tracks} is the number of tracks in one layer and N_{pulses} is the number of pulses for one track.

The number of tracks in one layer is expressed as:

$$N_{tracks} = (W/D_s) + 1 \tag{8}$$

where D_s is the track distance between two adjacent laser tracks.

The number of pulses for one track of length, L, is given by:

$$N_{pulses} = \frac{L}{A} \tag{9}$$

where A is the distance between the centres of two successive laser pulses.

The value A is simply given by:

$$A = \frac{V}{f} \tag{10}$$

where V is the scanning speed and f is the pulse repetition frequency.

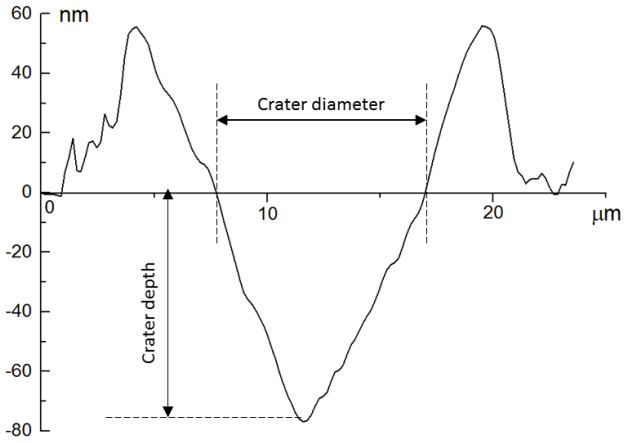

Fig.3. Schematic diagram of the method used to evaluate the diameter and depth of the crater

3. Results and discussion

3.1 Single pulse study

Fig. 4 shows the predicted thermal history on the surface of the BMG for different single pulses with various durations of 65 ns, 140 ns and 220 ns for a fixed laser fluence of 30 J/cm^2. The typical topography of a single crater for each laser irradiation condition is also included in this figure. As the heat source is assumed to follow a Gaussian distribution in space, the peak temperature is thereby in the centre of the laser spot. Hence, this point was always chosen to plot the data shown in this study for analysing the temperature evolution during laser machining. The theoretical model predicted that the surface temperature under all these three laser conditions reached values above the melting point. This is confirmed by the SEM micrographs also shown in Fig. 4. In particular, it can be seen from this figure that melt pools were formed on all specimens and that the melted material could also be either partially or completely ejected from the craters. This is indicative of the formation of recoil pressure caused by the vapour from the melt pool. The partially ejected material is located on the edge of the crater and is still in contact with the solidified melt pool due to the surface tension force opposing its separation. Completely ejected material re-solidified outside the crater. The plotted data also show that under a fixed laser fluence, the peak temperature decreases as the pulse duration increases. This is a result of the higher peak power at lower pulse length. On the other hand, a reduced pulse duration led to a slight decrease in diameter of the melted region. This should be due to the fact that a longer pulse provides more time available for the heat to propagate within the substrate and thus, for a larger volume of material to reach a temperature above the melting point.

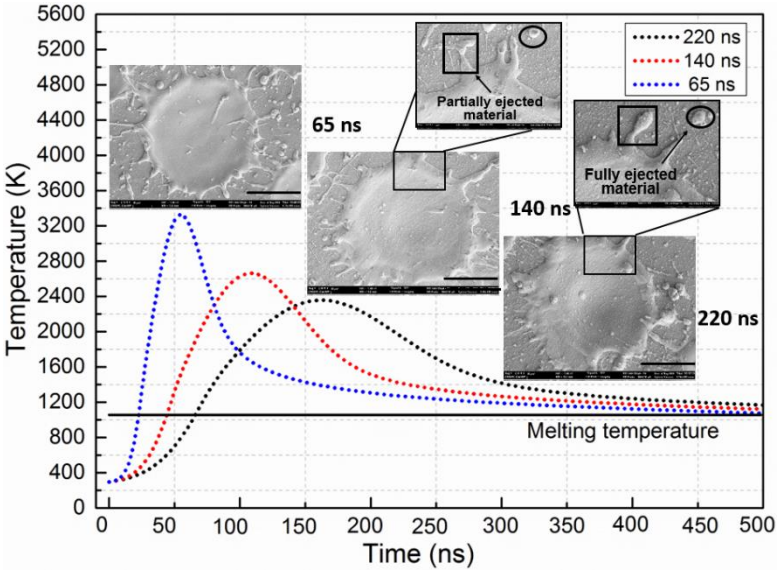

Fig. 4. Simulated temporal thermal evolutions at a fluence of 30 J/cm^2 for pulse durations of 65 ns, 140 ns and 220 ns. The inset SEM micrographs show the corresponding topography of the single craters. The horizontal line shows the melting temperature. Scale bars: 30 µm

The SEM micrograph displayed in Fig. 5 provides more detailed surface topography data following single pulse ablation with a duration of 65 ns at 30 J/cm^2. In particular, several laser-induced topographical features are reported in Fig. 5(b), which include partially and fully ejected melt, surface ripples and vapour condensates. As suggested by the simulation data plotted earlier in Fig. 4 under this specific laser processing condition, the surface temperature rises over 3000 K rapidly. This fast heating rate leads to the melt and vaporisation of the surface layer and the formation of a melt pool. In fact, the irradiance is estimated to be 4.6 x 10^8 W/cm^2 in this case, which may also initiate the formation of plasma (Steen and Mazumder, 2010). The recoil pressure over the melt pool leads to the ejection of molten material, leaving behind liquid droplets in a direction from the inside to the outside of the crater. The region of vaporised particles that condensed back onto the surface is observed both on and outside the re-solidified crater. The surface ripples could be attributed to effects taking place on the surface as well as within the material. The surface effect may be due to the Kelvin-Helmholtz (KH) instability, which has been discussed by Liu et al. (2011) in the case of Vitreloy 1. More specifically, KH-induced ripples features are typically generated at the interface between two fluids as a result of differences in their densities and velocities. For the work reported here, one of the fluids could be the vapour or plasma plume and the other fluid would be the BMG material in its supercooled liquid state. Fig. 5(c) illustrates the supercooled liquid region (SLR), which should form between the melt pool and the solid phase of the BMG. A second possible effect for the formation of ripples could be taking place within the material, also as a result of the recoil pressure. This pressure generates a radial force on the entire surface of the melt pool, which may be enough to “squeeze” the SLR. However, further work is necessary to test the validity of this hypothesis. Regardless of the specific cause for the formation of ripples, it is likely to be a consequence of the deformation of the material in the SLR. Using the thermal model developed in this study, it is estimated that the radial distance from the centre of the crater until the end of the SLR is 23 µm. As shown in Fig. 5(d), this boundary corresponds to the isotherm for which the temperature is equal to T_g. This theoretical value is in relatively good agreement with the radial distance of 26 µm, measured experimentally from the SEM data, until the point where the surface ripples extend. Interestingly, no ripple patterns could be noticed on the specimens treated with longer pulses. Based on data displayed earlier in Fig. 4, it is likely that this is due to a combination of two factors: (1) the longer pulse duration induced more material to be ejected from the melt pool and then to redeposit on the surface, possibly covering the ripple patterns and (2) the peak temperature of the material achieved with the longer pulse duration is lower than that reached with the shorter pulse length of 65 ns, which may affect the recoil pressure of the plume.

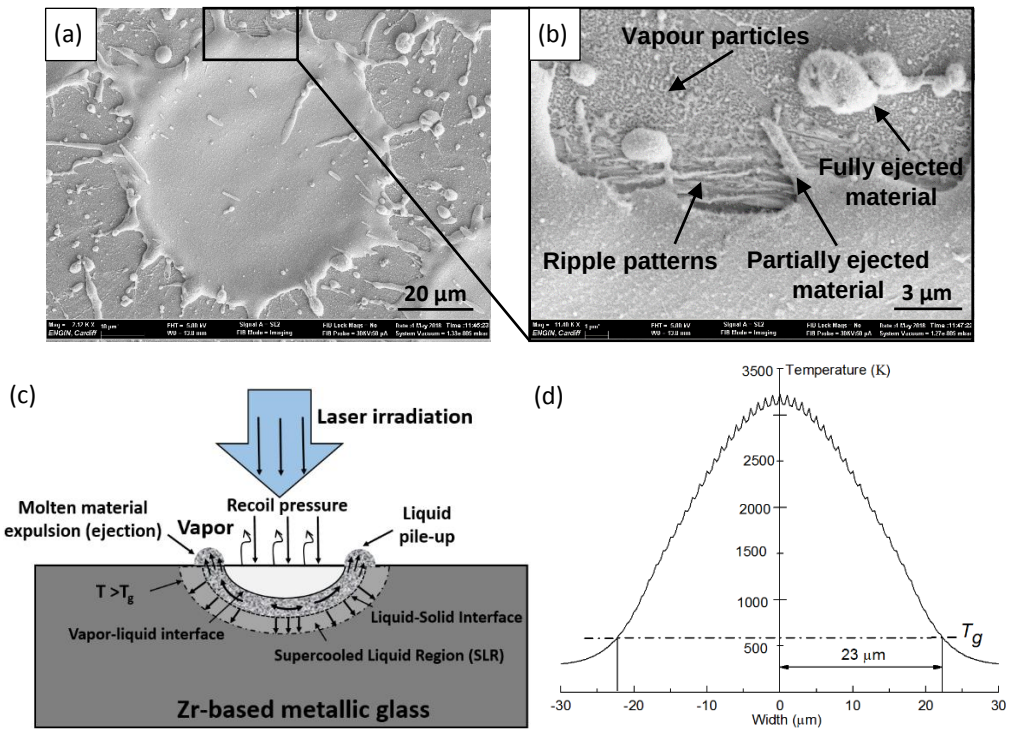

Fig. 5. (a) Full view and (b) close-up view of the surface topography of a crater on the Zr-based BMG resulting from single laser pulse irradiation at 65 ns and 30 J/cm^2, (c) schematic diagram of the laser-material interaction process (d) predicted spatial temperature distribution on the centre of the irradiated spot based on the developed thermal model for irradiation at 65 ns and 30 J/cm^2.

Fig. 6(a) shows the measured and simulated crater diameter and depth as a function of the laser fluence under the pulse duration of 220 ns. The simulated results were obtained by tracking the melt front and by assuming that all the melted material was removed from the crater. In spite of this simplifying assumption, it can be seen that the theoretical and experimental data generally agree quite well, except for the lowest fluence of 10 J/cm^2 and the higher fluence of 70 J/cm^2. In the first case, this discrepancy is most likely due to the fact that limited melt expulsion occurs at low fluence, which in turn would naturally result in simulated data overestimating the crater size, as is the case in Fig. 6(a). This is also confirmed from the AFM topography displayed with Fig. 6(b) where no splash or droplet can be observed around the crater. Instead, a circular rim is visible on its edge which is caused by the hydrodynamic motion of the liquid phase. This motion is a consequence of the action from the vapour pressure on the melt and also, it results from the gradient in the surface temperature of the melt along the radial direction of the crater. In the second case, i.e. at the higher fluence of 70 J/cm^2, the discrepancy between the simulated and measured data, especially for the depth, could be the result of the possible formation of plasma, which would attenuate the delivered energy from the incident laser beam. Overall, it can also be observed that the data plotted in this figure follow an increasing trend when the laser fluence is raised and then, the rate of this increase tends to reduce after 30 J/cm^2 for the diameter and 40 J/cm^2 for the depth. This reduction in energy efficiency occurs when the ablation process change form a melt-dominated to a vaporisation-dominated mechanism. This is also coupled with the possible initiation of plasma at the higher laser fluence values considered here. In addition to the discussion reported above regarding the discrepancies for the lowest and highest fluence data, it is also worth noting that between these two points, the predicted crater size is always a bit larger than the measured one. This may be due to a number of modelling assumptions, which have been made in this study. These include 1) the fact that the actual temporal beam shape of the fibre laser used is not Gaussian, 2) the thermal conductivity value employed being that of Vitreloy 1 and 3) the effect of the recoil pressure and surface tension force not having been taken into account. Fig. 6(c) and (d) show the AFM topography of single craters for the fluence values of 30 and 40 J/cm^2, respectively. Fig.7 shows the corresponding section profile of a single crater corresponding to Fig. 6(b), (c) and (d). The restricted range of motion for the AFM instrument utilised did not allow the scan to extend to areas where the droplets redeposited outside the crater. However, this was already observed with Fig. 5 in the case of

the 30 J/cm^2 laser irradiation. In summary, given the single pulse data reported here and based on cost and efficiency considerations for potential micromachining applications, laser irradiation with 220 ns pulse length at 30 J/cm^2 is selected to conduct the subsequent multiple laser pulse operations.

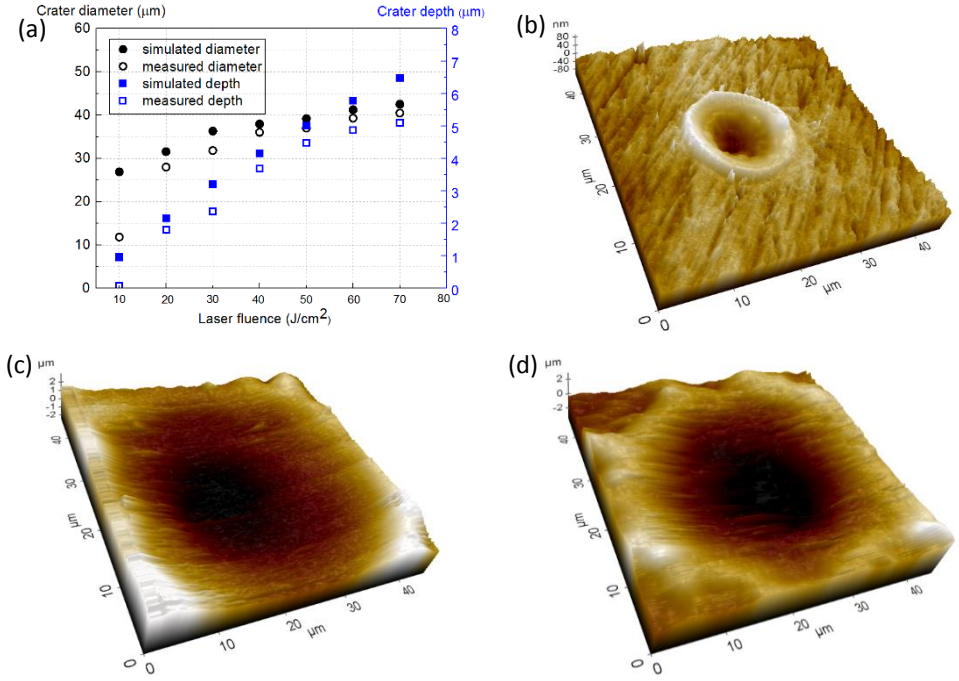

Fig. 6. (a) Simulated and experimental crater diameter and depth as a function of the laser fluence for a pulse duration of 220 ns and AFM scans of a single crater generated with the laser fluence of (b) 10 J/cm^2, (c) 30 J/cm^2 and (d) 40 J/cm^2.

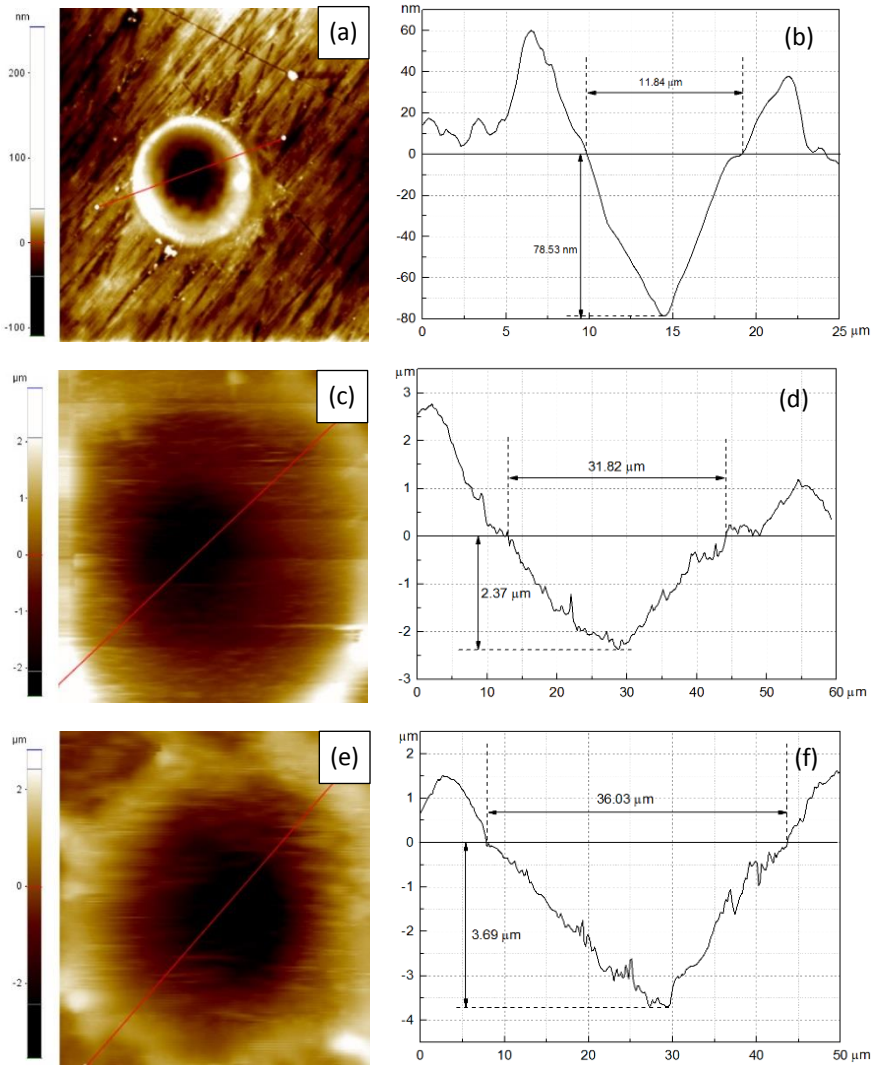

Fig.7 Location of cross-sections and corresponding profiles of single craters generated with the laser fluence of (a, b) 10 J/cm^2, (c, d) 30 J/cm^2 and (e, f) 40 J/cm^2

3.2. Multiple pulse study

In this section, the effect of the scanning speed on the surface topography of individual machined tracks is investigated. Fig. 8 shows secondary electron SEM micrographs of the Vitreloy 105 specimens with individual parallel tracks processed under a fixed laser fluence and pulse duration, i.e. 30 J/cm^2 and 220 ns, but using different scanning speeds, namely 100, 200 and 300 mm/s. These corresponded to a pulse overlap of 91.1%, 82.1% and 73.2%, respectively. In addition, Fig. 9 shows the corresponding back-scattered electron micrographs from Fig. 8. In all cases, it is observed that the area between the laser tracks is a region dense in liquid droplets made of re-solidified molten material ejected from the grooves. In Fig. 8(b), 8(d) and 8(f), it can also be seen that pores are formed within the micro-grooves, particularly for the lower scanning speed. These are caused by the viscous nature of the molten material during solidification. The distance between two adjacent laser tracks was 90 µm, which is much larger than the diameter of a single crater. This distance of 90 µm was set to eliminate the effect of the track distance on the surface topography and thus, to analyse results based on single groove data and observations. Qualitatively, it can be seen from Fig. 8 that protrusions on the edge of the grooves, caused by the re-solidification of laser-induced molten material, are quite prominent for the lowest

scanning speed of 100 mm/s (see Fig. 8(a)). This results from the highest overlap between laser pulses, which in turn, increases the number of repeated cycles of melt expulsion for a given irradiated area along the track. This can be seen with the theoretical temperature data displayed in Fig. 10, which reports the simulated successive heating and cooling cycles for a given point on the surface of the BMG specimen. In particular, this figure shows that a laser irradiated area always had enough time to fully solidify before the next incident laser pulse for the frequency used during this study, i.e. 35 kHz.

Fig. 11 shows the topography of the machined grooves for the different scanning speeds considered. For the lowest scanning speed of 100 mm/s, the average width of the protrusion was found to be 22.8 µm. With an increase in laser scanning speed to 300 mm/s, the width of the protrusions was found to decrease to 17.2 µm. The simulation results reported in Fig. 10 also show that the temperature of the first irradiated site rises to 2300 K (Fig. 10(c)), 2150 K (Fig. 10(b)) and 1950 K (Fig. 10(a)) upon the delivery of the second laser pulse, for scanning speeds of 100 mm/s, 200 mm/s and 300 mm/s, respectively. Hence, with an increase of the scanning speed from 100 mm/s to 300 mm/s, the effect of a subsequent laser pulse is reduced with respect to the induced temperature rise. As a result, the amount of molten material ejected from the melt pool is also reduced. Consequently, the width of the protrusion also decreases with the increase in scanning speed. In addition, based on the data displayed in Fig. 11, the average width of the grooves was measured to be 29.4 µm, 29.4 µm and 30.87 µm while the depth was 27.33 µm, 11.33 µm and 8.2 µm, for increasing values of scanning speed considered here. Moreover, it can also be observed qualitatively from the SEM micrographs that the depth decreases with the increase of scanning speed. Compared to a single pulse generated under the same laser fluence and pulse duration, the widths of the groove under different scanning speeds are a slightly smaller than that of the single pulse while their depth values are much larger.

A number of comments can be made based on the observation of the back-scattered electron SEM micrographs shown in Fig. 9. In particular, a qualitative analysis can be made with respect to the presence of regions with darker contrast. Such contrast should be indicative of a lighter elemental composition and in the context of this study, this could provide clues about the presence of oxides given that the laser processing experiments were conducted in ambient air. Although the scope of this paper is not concerned with the analysis of the effect of the laser processing on the resulting microstructure of the Vitreloy 105 specimens, it is useful to keep in mind that the presence of oxygen impurities promotes the recrystallization of a glassy alloy during solidification from the melt (Lin et al., 1997). From a purely qualitative comparison of Fig. 9(c) and Fig. 9(e), there seems to be a slightly more pronounced contrast between the centreline of a groove and the protrusion at its edge when the scanning speed increases from 200 mm/s to 300 mm/s. This may suggest that a reduced scanning speed could favour the introduction of oxide impurities. These possible phenomena would need further investigations in the future but in theory, this would be in-line with the fact that a lower scanning speed leads to a higher density of heating cycles above the melt temperature for a given region as observed with the output from the thermal model reported with Fig. 10. A closer examination of the surface of the grooves reveals that the darker regions are composed of cotton-like vapour particles. This observation is similar to data presented by Gasper et al. (2018). In particular, these authors reported that vapour nano-particles which were formed during laser powder bed fusion (LPBF) contained almost one-third of the element oxygen. This happened even when the process was conducted in a controlled environment with less than 0.1% oxygen. However, in contrast with this LPBF work, the re-solidified droplets observed in Fig. 9 do not seem to exhibit any dark patches on their surfaces, which would reveal the formation of discrete oxide spots on the droplets themselves. This may be due to the fact that, the LPBF process is typically conducted either with a continuous wave laser or in the microsecond regime and thus, with a much larger pulse length than that used here. Interestingly, the re-solidified droplets, which can be seen in Fig. 9, are covered by such cotton-like vapour particles regardless of the scanning speed utilised.

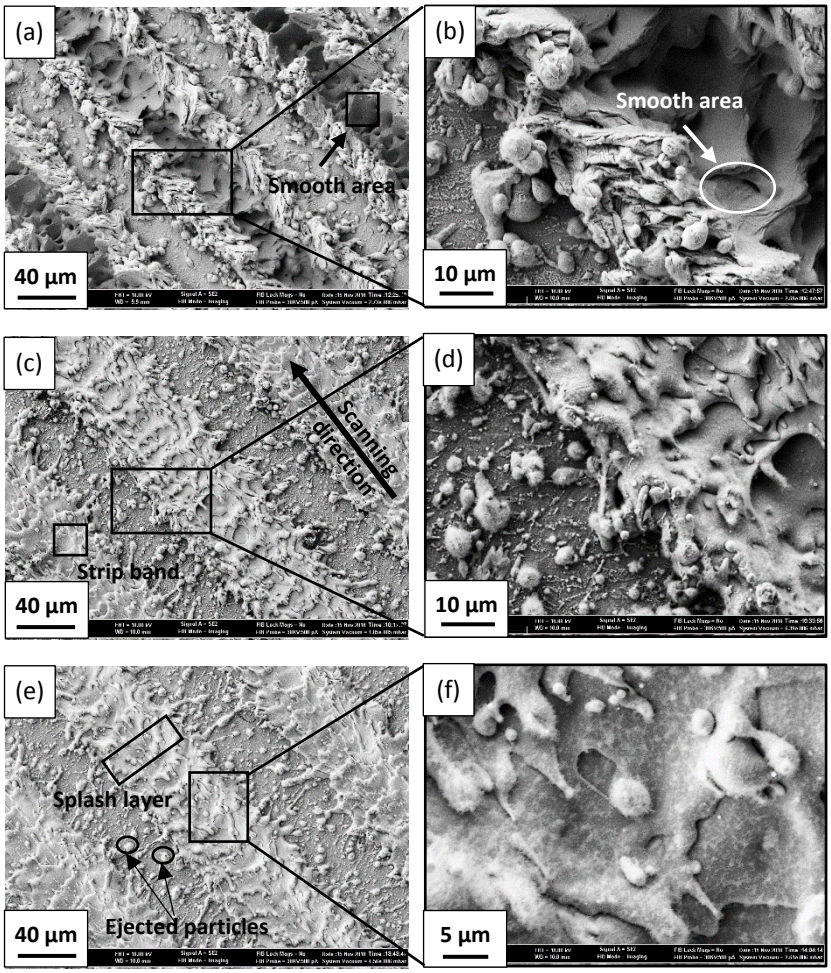

Fig. 8. Secondary electron SEM micrograph on the surface of laser machined grooves for different scanning speed values of (a, b) 100 mm/s, (c, d) 200 mm/s and (e, f) 300 mm/s. The figures (b), (d) and (f) are the corresponding enlarged views on selected regions of figures (a), (c) and (e).

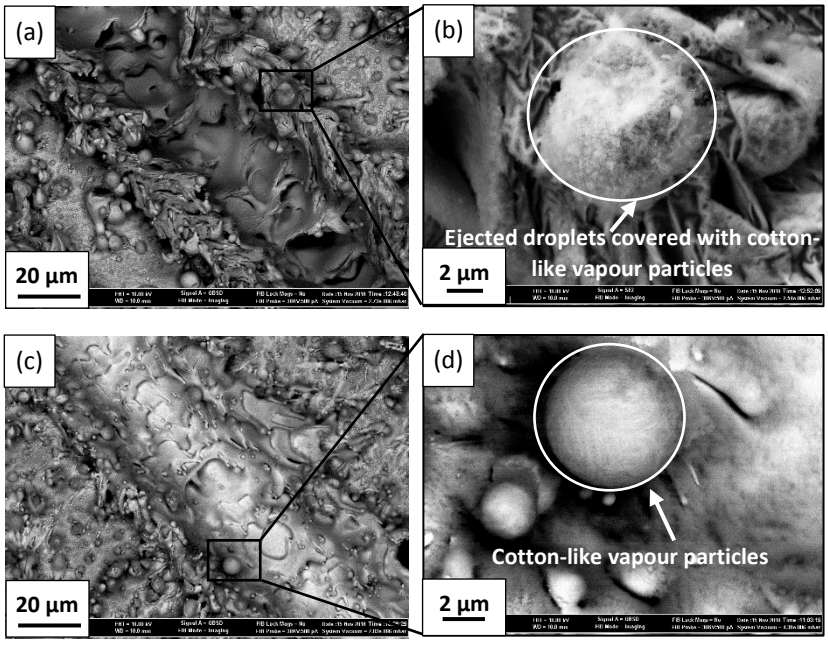

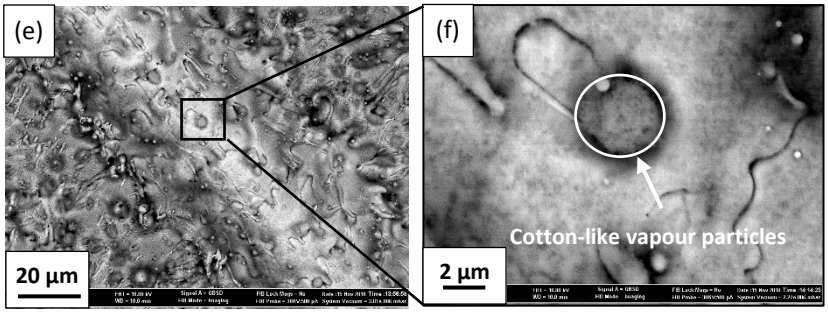

Fig. 9. Back-scattered electron micrographs on the surface of laser machined grooves for different scanning speed of (a, b) 100 mm/s, (c, d) 200 mm/s and (e, f) 300 mm/s. The figures (b), (d) and (f) are the corresponding enlarged views on selected regions of figures (a), (c) and (e).

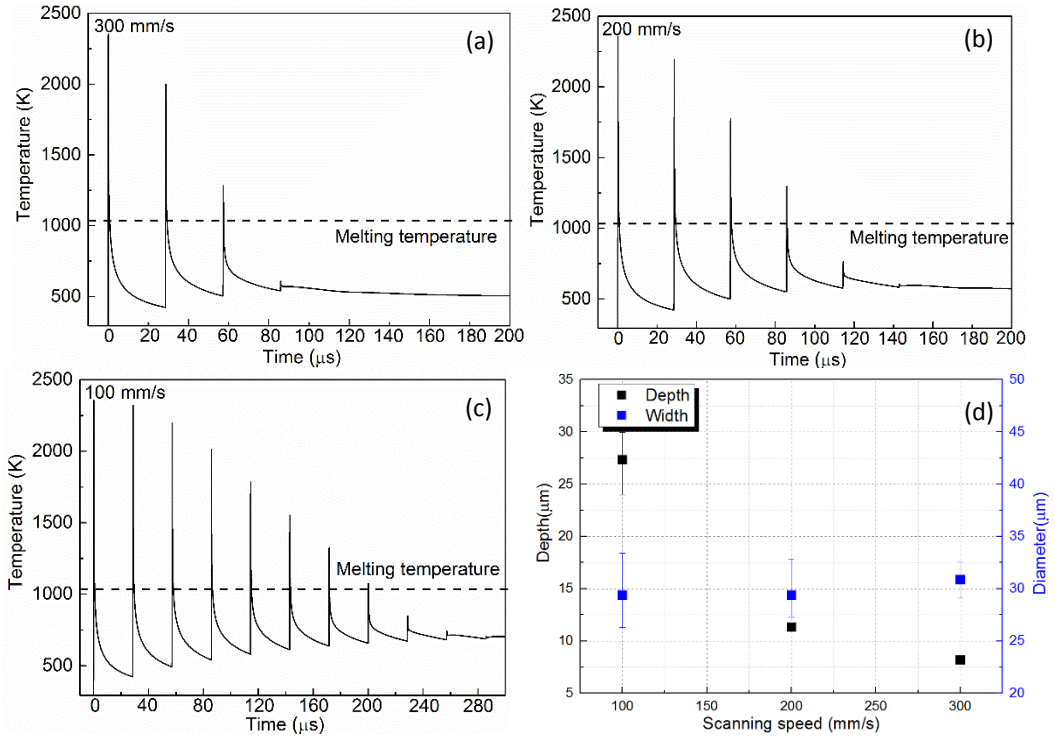

Fig. 10. Simulated temperature evolution during multiple laser irradiation with different scanning speeds of (a) 300 mm/s, (b) 200 mm/s and (c) 100 mm/s

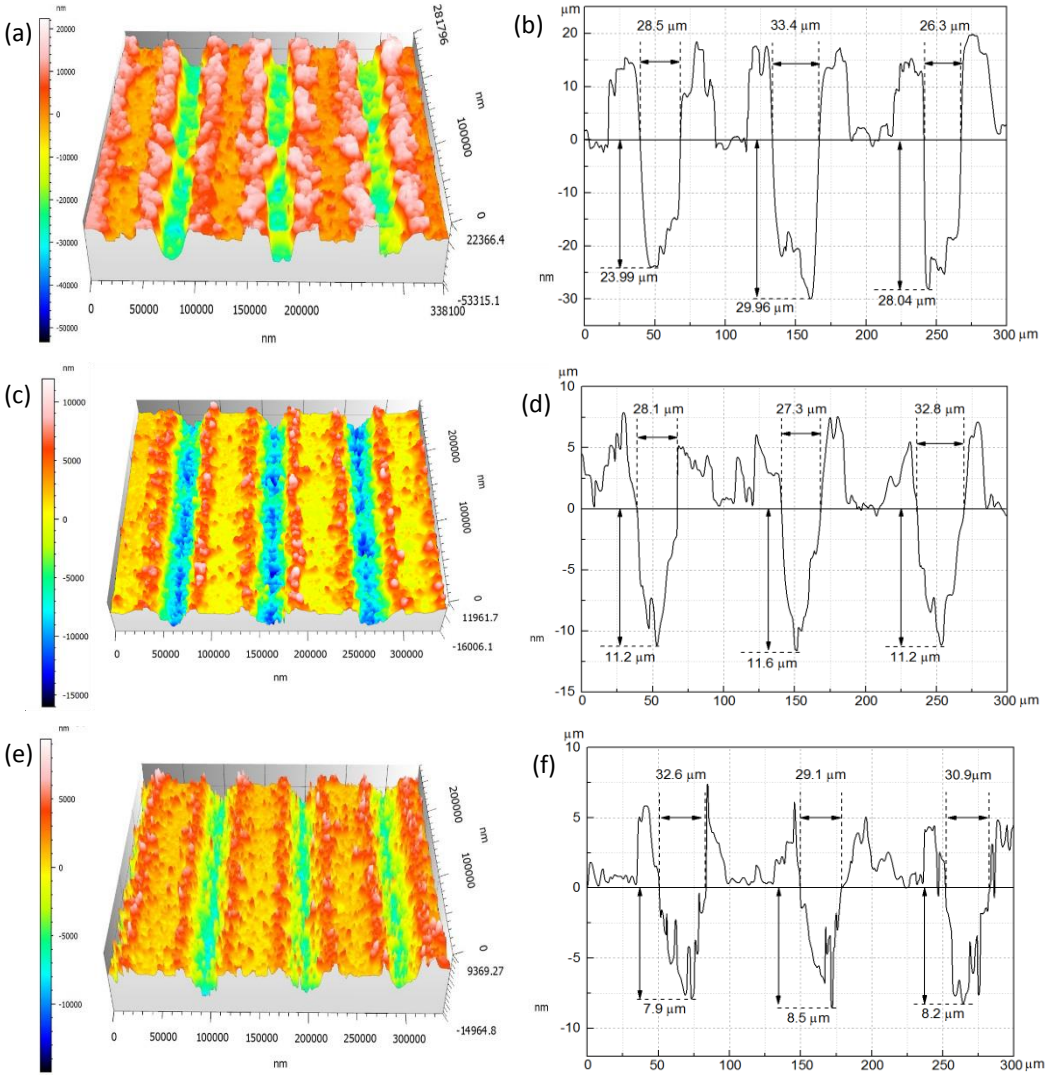

Fig.11. 3D profiles and their corresponding section profiles of the groove generated with the scanning speed of (a, b) 100 mm/s, (c, d) 200 mm/s and (e, f) 300 mm/s

3.3 Machining efficiency

A final set of experiments was conducted to investigate the effect of the track distance on the machining efficiency. The material removal rate (MRR), calculated with eq. (6), was used as an indicator of the machining efficiency. Pockets with dimensions 2.4 mm x 1.2 mm were milled with a 220 ns pulse and based on the results obtained in the previous sections, a fluence of 30 J/cm^2 and a scanning speed of 200 mm/s were selected. Given the pulse repetition frequency utilised, i.e. 35 kHz, this means that the overlap between two adjacent pulses along a track was 82% (with respect to the diameter of the laser spot size) and hence, that the specific distance between the centre of two consecutive pulses was 5.76 um (c.f. eq. (10)). The total number of laser pulses, N_{pulses}, required to machine a single track was 411 (eq. (9)). The required number of tracks, N_{tracks}, was calculated using eq. (8). MRR results against track distances values comprised between 5 µm and 15 µm are shown in Table 4 together with the measured depth achieved for one layer. Compared to the single line scan, the removed depth of the cavity is lower than that of the equivalent groove. This can be attributed to the fact that the protrusions created on the side of a single groove can lower the removing efficiency of the subsequent groove as these protrusions are not positioned at the focal point of the laser beam (Huang et al, 2017). The range of track distance values considered here corresponds to a track overlap comprised between 84.4% and 53.1%. It can be seen from Table 4 that the removed depth decreases with the increase in track distance

as one would expect, similarly to the observations made earlier in the case of varying pulse overlaps along a groove. Overall, with the increase in track distance, the removed depth reduces, which in turn lowers the removed volume of material for one layer, while at the same time, the processing time decreases which has the opposite effect on the MRR. In the experimental window reported in Table 4, the MRR always increases with the increase of track distance. This means that the decrease of processing time dominates the evolution of the MRR.

Table 4. MRR values achieved as a function of the track distance

Track distance, D_s (µm)	Percentage overlap between tracks	Removed depth for one layer, d (µm)	Total processing time, $t_{processing}$ (ms)	*MRR* (mg/s)
5	84.4%	9.03	21.79	8.03
7	78.1%	8.43	15.64	10.45
10	68.8%	8.15	10.85	14.56
12	62.5%	7.63	9.04	16.36
15	53.1%	7.04	7.23	18.87

4. Conclusions

Given the potential application of laser processing for the manufacture of BMG micro-components, this study combined theoretical and experimental investigations in a micromachining context, i.e. when multiple and moving pulse irradiations are applied. In particular, a nanosecond pulsed fibre laser system was employed to process a Zr-based amorphous alloy, also known as Vitreloy 105. The material response during single and multiple pulse processing was studied under different parameters both theoretically and experimentally when considering laser material interaction phenomena and the evolution of simulated temperature data.

The output of the theoretical model showed a good agreement with the experimental results when analysing the dimensions of single craters. Besides, the simulated spatial temperature data could also be used to predict the width of the supercooled liquid region underneath the melt pool. Thus, the developed model was subsequently applied to multiple and moving pulses operations for interpreting experimental observations made about the effect of the scanning speed on micro-groove size and topography. In this case, it was seen that for the pulse repetition frequency utilised in this study, i.e. 35 KHz, the laser irradiated area had ample time to solidify before the next incident laser pulse, regardless of the scanning speed value selected. Thus, the Vitreloy 105 substrate was always subjected to repeated cycles of heating and cooling from its solid state. Such information should be taken into account in future studies where the microstructure evolution of BMG specimens is investigated in a laser micromachining scenario. In particular, such thermal cycles result in non-standard conditions when considering crystal nucleation phenomena compared to the conventional synthesis of glassy alloys from the liquid state. In addition, the fact that vapour nano-particles were relatively easily formed under all scanning speeds should lead to increase the likelihood of oxygen impurities diffusing into the melt pool, which in turn, should affect the crystallisation kinetic. Finally, the effect of different track distances on the material removal rate was also investigated. It was found that the evolution of the material removal rate, for the fluence and pulse duration values identified, was dominated by the processing time rather than by variation in the volume of removed material.

Acknowledgements

The authors would like to thank Mr Marco Santonastaso from the CLEER lab at Cardiff University for his assistance in the sample preparation and XRD measurement; Mr Xiaojun Shen from Coventry University for the discussion about the XRD results; Mr Paul Stewart from CEA LETI, Grenoble, France, for the AFM measurements; Mr William Britton from the Tribology and Performance of Machines, Structures and Materials Research Group at Cardiff University for helping with Talysurf measurements and Dr Debajyoti Bhaduri from Cardiff University for assistance with the Sensofar 3D optical microscope. The lead author (Yang Jiao) gratefully appreciates the financial support from Cardiff University, UK and Xi'an Jiaotong University, China. Emmanuel Brousseau gratefully acknowledges the financial support

provided by the Welsh Government and Higher Education Funding Council for Wales through the Sêr Cymru National Research Network in Advanced Engineering and Materials.

References

Ashby, M.F., Greer, A.L., 2006. Metallic glasses as structural materials. Scripta Materialia 54(3), 321-326.

Bian, Z., Pan, M.X., Zhang, Y., Wang, W.H., 2002. Carbon-nanotube-reinforced bulk metallic glass composites. Applied Physics Letter 81(25), 4739-4741.

Chen, B.Q., Pang, S.J., Han, P.P., Li, Y., Yavari, A.R., Vaughan, G., Zhang, T., 2010. Improvement in mechanical properties of a Zr-based bulk metallic glass by laser surface treatment. Journal of Alloys and Compounds 504(S1), S45–S47.

Chen, M.W., 2011. A brief overview of bulk metallic glasses. NPG Asia Materials 3, 82-90.

Cheng, Y.Q., Ma, E., 2011. Intrinsic shear strength of metallic glass. Acta Materialia 59, 1800-1807.

Chen, Y.C., Chu, J.P., Jang, J.S.C., Hsieh, C.W., Yang, Y., Li, C.L., Chen, Y.M., Jeng, J.Y., 2013. Replication of nano/micro-scale features using bulk metallic glass mold prepared by femtosecond laser and imprint processes. Journal of Micromechanics and Micro-engineering 23, 035030.

Demetriou, M.D., Johnson, W.L., 2004. Modelling the transient flow of undercooled glass-forming liquids. Journal of Applied Physics 95(5), 2857–2865.

Fu, J., Zhu, Z., Zheng, C., Liu, R., Ji, Z., 2014. Effect of laser shock peening on mechanical properties of Zr-based bulk metallic glass. Applied Surface Science 313, 692–697.

Glade, S.C., Busch, R., Lee, D.S., Johnson, W.L., Wunderlich, R.K., Fecht, H.J., 2000. Thermodynamics of $Cu_{47}Ti_{34}Zr_{11}Ni_8$, $Zr_{52.5}Cu_{17.9}Ni_{14.6}Al_{10}Ti_5$ and $Zr_{57}Cu_{15.4}Ni_{12.6}Al_{10}Nb_5$ bulk metallic glass forming alloys. Journal of Applied Physics 87(10), 7242-7247.

Gasper, A.N.G., Szost, B., Wang, X., Johns, D., Sharma, S., Clare, A.T., Ashcroft, I. A., 2018. Spatter and oxide formation in laser powder bed fusion of Inconel 718. Additive Manufacturing 24, 446-456.

Hitz, B., Ewing, J.J., Hecht, J., 2005. Introduction to Laser Technology. Wiley, New Jersey.

Huang, H., Yan, J.W., 2017. Surface patterning of Zr-based metallic glass by laser irradiation induced selective thermoplastic extrusión in nitrogen gas. Journal of Micromechanics and Microengineering 27, 075007.

Inoue, A., Takeuschi, A., 2011. Recent developments and application products of bulk glassy alloys. Acta Materialia, 59(6), 2243-2267.

Inoue, A., Kong, F.L., Man, Q.K., Shen, B.L., Li, R.W., Al-Marzouki, F., 2014. Development and applications of Fe- and Co- based glassy alloys and their prospects. Journal of alloys and compounds 615(S1), S2-S8.

Johnson, W. L., 1999. Bulk Glass-Forming Metallic Alloys: Science and Technology. MRS Bulletin 24(10), 42-56.

Jiang, M.Q., Wei, Y.P., Wilde, G., Dai, L.H., 2015. Explosive boiling of a metallic glass superheated by nanosecond pulse laser ablation. Applied Physics Letters 106(2), 021904.

Kim, J., Lee, D., Shin, S., Lee, C., 2006. Phase evolution in $Cu_{54}Ni_6Zr_{22}Ti_{18}$ bulk metallic glass Nd:YAG laser weld. Material Science and Engineering: A 434(1-2), 194–201.

Kannatey-Asibu, E., 2009. Principles of Laser Materials Processing, John Wiley & Sons.

Kolev, N.I., 2015. Thermo-physical properties for severe accident analysis. Multiphase Flow Dynamics 5, 617–807.

Kuriakose, S., Patowari, P.K., Bhatt, J., 2017. Machinability study of Zr-Cu-Ti metallic glass by micro hole drilling using micro-USM. Journal of Materials Processing Technology 240, 42-51.

Loffler, J.F., 2003. Bulk metallic glasses. Intermetallics 11(6), 529-540.

Lin, X.H., Johnson, W.L., W.K. Rhim, 1997. Effect of oxygen impurity on crystallization of an undercooled bulk glass forming Zr-Ti-Cu-Ni-Al alloy. Materials Transactions, JIM 38(5), 473-477.

Liu, Y., Jiang, M.Q., Yang, G.W., Guan, Y.J., Dai, L.H., 2011. Surface rippling on bulk metallic glass under nanosecond pulse laser ablation. Applied Physics Letters 99, 191902.

Liu, W.D., Ye, L.M., Liu, K.X., 2011. Micro-nano scale ripples on metallic glass induced by laser pulse. Journal of Applied Physics 109(4), 043109.

Lin, H.K., Lee, C.J., Hu, T.T., Li, C.H., Huang, J.C., 2012. Pulsed laser micromachining of Mg-Cu-Gd bulk metallic glass. Optics and Lasers in Engineering 50(6), 883-886.

Liu, J.M., 1982. Simple technique for measurements of pulsed Gaussian-beam spot sizes. Opt. Lett. 7 (5), 196–198.

Ma, F.X., Yang, J.J., Zhu, X.N., Liang, C.Y., Wang, H.S., 2010. Femtosecond laser-induced concentric ring microstructures on Zr-based metallic glass. Applied Surface Science 256(11), 3653-3660.

Naleway, S.E., Greene, R.B., Gludovatz, B., Dave, N.K.N., Ritchie, R.O., Kruzic, J.J., 2013. A highly fatigue-resistant Zr-based bulk metallic glass. Metallurgical and Materials Transactions A 44(13), 5688-5693.

Nie, X.F., He, W.F., Zhou, L.C., Li, Q.P., Wang, X.D., 2014. Experiment investigation of laser shock peening on TC6 titanium alloy to improve high cycle fatigue performance. Materials Science and Engineering: A 594(31), 161-167.

Peter, W.H., Liaw, P.K., Buchanan, R.A., Liu, C.T., Brooks, C.R., Horton Jr, J.A., Carmichael Jr, C.A., Wright, J.L., 2002. Fatigue behaviour of Zr52.5Al10Ti5Cu17.9Ni14.6 bulk metallic glass. Intermetallics 10(11-12), 1125-1129.

Quintana, I., Dobrev, T., Aranzabe, A., Lalev, G., Dimov, S., 2009. Investigation of amorphous and crystalline Ni alloys response to machining with micro-second and pico-second lasers. Applied Surface Science 255(13-14), 6641-6646.

Ready, J.F., 1965. Effects Due to Absorption of Laser Radiation. Journal of Applied Physics 36(2), 462–468.

Samant, A.N., Dahotre, N.B., 2009. Laser machining of structural ceramics - A review. Journal of European Ceramic Society 29(6), 969-993.

Schroers, J., Desai, Q. P. A., 2007. Thermoplastic forming of bulk metallic glass – a technology for MEMS and Microstructure fabrication. Journal of Microelectromechanical systems 16(2), 240-247.

Steen, W. M. and Mazumder, J., 2010. “Laser drilling and Piercing,” in Laser Material Processing. Springer London, 131-198.

Steen, W. M., Mazumder, J., 2010. “Theory, Mathematical Modelling and Simulation,” in Laser Material Processing. Springer London, 251–294

Vora, H.D., Rajamure, R.S., Soundarapandian, S., Srinivasan, S., Dahotre, N.B., 2013. Dilution of molybdenum on aluminum during laser surface alloying. Journal of Alloys and Compounds 570, 133–143.

Vella, P.C., Dimov, S.S., Brousseau, E.B., Whiteside, B.R., 2015. A new process chain for producing bulk metallic glass replication masters with micro- and nano-scale features. International Journal of Advanced Manufacturing Technology 76(1-4), 523-543.

Wang, W.H., Dong, C., Shek, C.H., 2004. Bulk metallic glasses. Material Science and Engineering R: Reports 44(2-3), 45-89.

Wang, X.L., Lu, P.X., Dai, N.L., Li, Y.H., Liao, C.R., Zheng, Q.G., Liu, L., 2007. Noncrystalline micromachining of amorphous alloys using femtosecond laser pulses. Materials letters 61(21), 4290-4293.

Wang, C., Zeng, X., 2007. Study of laser carving three-dimensional structures on ceramics: Quality controlling and mechanisms. Optics and Laser Technology 39(7), 1400–1405.

Williams, E., Brousseau, E.B., 2016. Nanosecond laser processing of $Zr_{41.2}Ti_{13.8}Cu_{12.5}Ni_{10}Be_{22.5}$ with single pulses. Journal of Materials Processing Technology 232, 34-42.

Williams, E., Lavery, N., 2017. Laser processing of bulk metallic glass: A review. Journal of Materials Processing Technology, 247, 73-91.

Yang, G., Lin, X., Liu, F., Hu, Q., Ma, L., Li, J., Huang, W., 2012. Laser solid forming Zr-based bulk metallic glass. Intermetallics 22, 110–115.

Zhang, L., Pauly, S., Zhu, Z.W., Gemming, T., Fu, H.M., Eckert, J., Zhang, H.F., 2016. Ion milling-induced micrometer-sized heterogeneities and partial crystallization in a TiZrCuFeBe bulk metallic glass. Intermetallics 73, 5-11.

Zhang, Y., Liu, H.S., Mo, J.Y., Wang, M.Z., Chen, Z., He, Y.Z., Yang, W.M., Tang, C.G., 2018. Atomic-scale structural evolution in selective laser melting of $Cu_{50}Zr_{50}$ metallic glass. Computational Materials Science 150, 62-69.

Zhu, Y.H., Fu, J., Zheng, C., Ji, Z., 2016. Effect of nanosecond pulse laser ablation on the surface morphology of Zr-based metallic glass. Optics & Laser Technology 83, 21-27.